# A Novel Fluid-Structure Interaction Framework for Flapping, Flexible Wings

# Ryan Schwab

Mechanical and Industrial Engineering, Montana State University, Bozeman, MT 59717 e-mail: rschwab03@gmail.com

# **Erick Johnson**

Assistant Professor Mechanical and Industrial Engineering, Montana State University, Bozeman, MT 59717 e-mail: erick.johnson@montana.edu

# Mark Jankauski<sup>1</sup>

Assistant Professor Mechanical and Industrial Engineering, Montana State University, Bozeman, MT 59717 e-mail: mark.jankauski@montana.edu

Fluid-structure interaction (FSI) plays a significant role in the deformation of flapping insect wings. However, many current FSI models are high-order and rely on direct computational methods, thereby limiting parametric studies as well as insights into the physics governing wing dynamics. We develop a novel flapping wing FSI framework that accommodates general wing geometry and fluid loading. We use this framework to study the unilaterally coupled FSI of an idealized hawkmoth forewing considering two fluid models: Reynolds-averaged Navier-Stokes computational fluid dynamics (RANS CFD) and blade element theory (BET). We first compare aerodynamic modal forces estimated by the loworder BET model to those calculated via high fidelity RANS CFD. We find that for realistic flapping kinematics, BET estimates modal forces five orders of magnitude faster than CFD within reasonable accuracy. Over the range flapping kinematics considered, BET and CFD estimated modal forces vary maximally by 350% in magnitude and approximately  $\pi/2$ radians in phase. The large reduction in computational time offered by BET facilitates high-dimensional parametric design of flapping-wing-based technologies. Next, we compare the contributions of aerodynamic and inertial forces to wing deformation. Under the unilateral coupling assumption, aerodynamic and inertial-elastic forces are on the same order of magnitude—however, inertial-elastic forces primarily excite the wing's bending mode whereas aerodynamic forces primarily excite the wing's torsional mode. This suggests that, via conscientious sensor placement and orientation, biological wings may be able to sense independently inertial and aerodynamic forces.

[DOI: 10.1115/1.4044268]

Keywords: aeroelasticity, dynamics, flow-induced vibration, flapping wing mechanics, fluid-structure interaction

## 1 Introduction

Micro air vehicles (MAVs) have become a pervasive technology over the past decade. They are considered for countless applications ranging from package delivery to storm tracking and forecasting. Many applications require MAVs to be very small so that they are able to negotiate dense, congested environments. For example, a MAV designed to identify leaks at gas refineries must be tiny enough to negotiate complex piping networks. Unfortunately, fixed-wing or rotor-based aircraft suffers inefficiencies at small scale that preclude their flight. Viscous forces tend to dominate lift-generating aerodynamic forces, and conventional rotary motors cannot effectively dissipate heat [1,2]. As a result, robotic designers generally rely on flapping wings as an alternative mechanism to produce lift and thrust at small scale. Flapping wing micro air vehicles (FWMAVs) are relatively new robotic platforms that have realized flight at centimeter lengths and milligram weights [3]. Many of these platforms are designed using flapping wing insects as inspiration. However, several issues preclude widespread realization of these insectinspired FWMAVs for useful tasks. These issues include inefficient energetics, heavy sensors, and material fatigue. A better understanding of insect flight, in particular, the flapping wing, can inform engineering design to overcome many of these technological challenges.

As an insect wing flaps, it bends and twists under both aerodynamic and inertial-elastic forces [4]. The interplay of aero and structural dynamics is called fluid–structure interaction (FSI). The wing's deformation is speculated to serve several important

functions, including energy management [5-7] and angular rate sensing [8]. Flexible wings offer higher lift-to-drag ratios relative to their rigid counterparts [9], suggesting wing deformation benefits aerodynamic power economy; flexibility is hypothesized to reduce inertial power requirements, as well. Unlike rigid wings, compliant wings store strain energy while flapping [10]. Much of this stored energy can be recruited to accelerate or decelerate the wing over a wingbeat, and this energy recycling mechanism improves inertial power economy [7]. Thus, wing compliance and deformation are central to the energy efficiency of small-scale biological flight. However, wing flexibility also provides a necessary sensing modality. Many insect wings are permeated with camaniform sensilla, a mechanoreceptor which responds to stress and strain [11]. The lowlatency mechanical feedback encoded by these receptors allows the insect to react quickly to environmental perturbations [8], such as wind gusts or collisions with plants. Given the multifaceted characteristics of insect wings, they are an ideal structure to emulate in bio-inspired technologies. Nevertheless, the fluid and structural dynamics of flapping, flexible insect wings are not well understood.

Much research in the area of insect flight focuses on experimental studies. In a seminal study, Combes and Daniel artificially flapped a hawkmoth *Manduca sexta* in both air and helium (≈15% the density of air) with single degree-of-freedom (SDOF) rotation [4]. The objective of this study was to identify if inertial-elastic or aerodynamic forces were primarily responsible for wing deformation. They used high-speed videography to track several points over the wing surface while flapping and compared the deflection of these points both in air and in helium. Interestingly, they observed that wing deformation was similar in both cases; the natural conclusion was that the wing's dynamic response was primarily a function of inertial-elastic forcing. Norris later conducted a similar study with two notable differences: the wing was actuated in coarse vacuum rather than helium, and the full-field displacement was

<sup>&</sup>lt;sup>1</sup>Corresponding author.

Contributed by the Technical Committee on Vibration and Sound of ASME for publication in the JOURNAL OF VIBRATION AND ACOUSTICS. Manuscript received December 6, 2018; final manuscript received July 15, 2019; published online July 31, 2019. Assoc. Editor: Maurizio Porfiri.

measured (at limited time steps) rather than displacement at individual points [12]. Contradictory to the findings of Combes and Daniel, Norris asserted that the contribution of fluid loading to the wing cannot safely be neglected. The conflicting results of these two studies suggest that the relative contribution of aerodynamic and inertial-elastic forces to wing deformation remains unknown.

To provide deeper insight into structural deformation and flapping wing FSI, many researchers rely on numerical simulation and modeling. Most flapping wing FSI models utilize coupled finite element analysis (FEA) and computational fluid dynamics (CFD) [13-16]. While such approaches accurately describe wing deformation and the surrounding flow field, the time required to generate a single solution is extensive. Both fluid and structural solvers suffer computational inefficiencies and these inefficiencies are compounded when the two physical regimes are considered together. For example, large wing rotations give rise to centrifugal and gyroscopic effects which cause the FEA stiffness matrix to be time-varying [17]. The stiffness matrix must be updated at each interval of analysis, and the result is an enormous number of degrees-of-freedom (DOFs) on the order of number of finite elements × number of time steps. Each physical DOF must be solved independently and the lengthy solution time makes direct FEA simulation in an impractical analysis method for dynamic systems subject to large rotation. CFD solvers, which typically rely on Reynolds-averaged Navier-Stokes (RANS) methods in the context of flapping flight, must resolve the flow field over an entire control volume to estimate the pressures on a wing. The extensive number of equations that must be solved and conditions that must be satisfied render CFD a computationally demanding mechanism. Therefore, given their computational demands, direct FSI models which leverage coupled CFD and FEA are not well suited for parameter studies.

To circumvent these computational issues, several methods were developed to study flapping wing flight more efficiently. The most common aerodynamic model is based upon blade element theory (BET), a quasi-steady approach that discretizes the wing into airfoils [18-20]. BET has been used to identify power-minimizing flapping kinematics [21], to explore the influence of inertial torques on insect steering [22], and to estimate passive pitch rotation in robotic vehicles [23]. However, while BET produces aerodynamic force estimates extraordinarily quickly, it is conventionally applied to rigid wings and is not widely used to study flapping wing FSI. Notable exceptions include works by Wang et al. [24] and Stanford et al. [25]. Wang developed a BET-based FSI model of twistable wings and showed that torsional flexibility improves power efficiency. However, their model was unable to account for spanwise bending. Stanford's FSI model was able to capture bending, but the discretization was limited to coarse chord-wise elements and could not account for the complex deformation modes observed in insect flight. Consequently, it is unknown if FSI models rooted in BET can adequately describe the realistic deformation of insect wings. We recognize that BET-FSI models and other reduced-order approaches have been used to describe other rotating systems influenced by aerodynamics, such as wind turbines and rotor blades [26–29]. However, the small length scale, high-frequency actuation, and multidimensional rotational kinematics of flapping insect wings render this a unique and challenging problem that has not been adequately addressed in a reduced-order fashion.

Given the motivation, there are two objectives of this paper: (1) evaluate the accuracy of a reduced-order flapping wing FSI model based upon BET and (2) identify the relative contribution of inertial-elastic and aerodynamic forces to wing deformation at a moth scale. To achieve these objectives, we develop a novel FSI model with the following characteristics. First, the model is general enough to accommodate arbitrary wing geometry and any fluid modeling scheme, including BET and CFD. Second, the model permits either unilateral or bilateral fluid–structure coupling. The general model derived here is the primary research contribution of this work. For the remainder of the paper, we stress that the primary interest is the physics governing structural deformation rather than the effect structural deformation has on the surrounding flow structure.

In this work, we consider only unilateral coupling, where the fluid affects the structure but the deforming structure does not affect the fluid. For unilateral coupling, aerodynamic forces are determined assuming wing rigidity and are subsequently applied to determine structural deformation. The assumption is most appropriate when wing deflections are small. To the best of our knowledge, there are no existing studies that compare the accuracy of unilaterally and bilaterally coupled FSI models of flapping wings. Thus, while this assumption may not be appropriate for the broad range of biological or artificial fliers, it is a suitable starting place to begin understanding the complex FSI of flapping wings. The unilateral approach enables us to study large parameter spaces more quickly than the bilateral approach, since the bilateral approach necessitates remeshing of the CFD grid at each interval of analysis. This assumption also helps us to identify under what parameters wing deformation becomes large enough to consider a bilaterally coupled analysis. For these reasons, we focus on unilateral FSI coupling for this work and will address bilateral FSI coupling in the future research. However, we acknowledge that some dynamic phenomena, for example, fluid damping, will not be present in the proposed unilateral approach.

The remainder of the paper is organized as follows. First, the aeroelastic framework is derived using the Lagrangian approach. Generalized aerodynamic loading is accounted for via the principle of virtual work. We then detail the BET and RANS CFD fluid models used in this research. The resulting aeroelastic framework is applied to study the FSI of a simulated hawkmoth wing. Then, we assess the accuracy of BET for hovering flight flapping kinematics and evaluating the sensitivity of BET as kinematics deviate from the hovering case. We next compare the relative contributions of aerodynamic and inertial-elastic forces to wing deformation. Lastly, we discuss our findings and how they are relevant to the design and optimization of FWMAVs as well as the study of biological flight.

## 2 Theory

We first develop a reference frame fixed to the rigid body motion of a flapping wing. We then derive the aeroelastic framework governing the wing modal response, where the structural response is determined via the Lagrangian formulation and nonconservative aerodynamic modal forces are accounted for through the principle of virtual work. We conclude by discussing the two aerodynamic loading models utilized in this work, specifically BET and RANS CFD.

**2.1 Aeroelastic Modeling.** The structural framework detailed in this section was originally developed by Jankauski and Shen [17]. However, the initial formulation assumed inertial-elastic forces were solely responsible for wing deformation—aerodynamic forces were neglected. While this assumption may be justified within the context, there are scenarios in which aerodynamic forces contribute nontrivially to deformation. Thus, the primary purpose of this work is to identify how aerodynamics affect the structural dynamics of flapping, flexible wings during hovering flight. The aeroelastic framework required to explore this subject is derived as follows.

Consider a wing of arbitrary geometry placed into an XYZ inertial coordinate frame (Fig. 1). The XYZ is rotated about the X axis with amplitude  $\alpha$ , where  $\alpha$  denotes roll. The subsequent x''y''z'' is rotated about the y'' axis with amplitude  $\beta$ , where  $\beta$  denotes pitch. The x'y'z' frame undergoes a final rotation about the z' axis with an amplitude  $\gamma$ , where  $\gamma$  denotes yaw. The origin of the terminal xyz frame is a fixed point. The terminal frame is bound to the rigid body motion of the wing and has an angular velocity

$$\vec{\Omega} = \underbrace{(\dot{\alpha}\cos\beta\cos\gamma + \dot{\beta}\sin\gamma)}_{\Omega_{x}} \vec{e}_{x} + \underbrace{(\dot{\beta}\cos\gamma - \dot{\alpha}\cos\beta\sin\gamma)}_{\Omega_{y}} \vec{e}_{y} + \underbrace{(\dot{\gamma} + \dot{\alpha}\sin\beta)}_{\Omega_{z}} \vec{e}_{z}$$
(1)

061002-2 / Vol. 141, DECEMBER 2019

**Transactions of the ASME** 

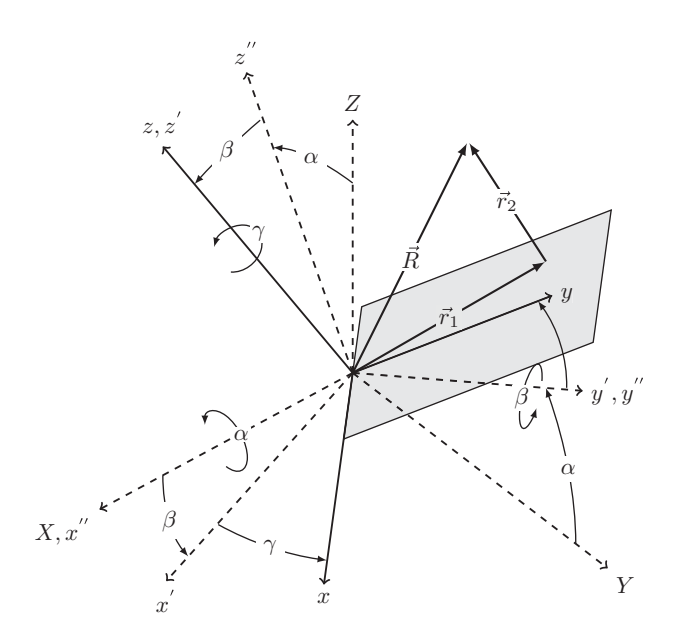


Fig. 1 Rotating reference frame attached to the rigid body motion of the wing

where  $\vec{e_x} - \vec{e_y} - \vec{e_z}$  are unit vectors along the rotated frames x–y–z axes and  $\Omega_x$ ,  $\Omega_y$ , and  $\Omega_z$  are the components of the angular velocity vector. Next, a position vector  $\vec{R}$  is drawn from the fixed reference frame origin to a differential mass dm. For convenience, the position vector  $\vec{R}$  is represented as  $\vec{R} = \vec{r_1} + \vec{r_2}$ , where

$$\vec{r_1} = x\vec{e_x} + y\vec{e_y} \tag{2}$$

$$\vec{r}_2 = W(\vec{r}_1, t)\vec{e}_7 \tag{3}$$

Above,  $\vec{r_1}$  represents the planar coordinates of dm with respect to the undeformed wing and  $\vec{r_2}$  represents a infinitesimal out-of-plane elastic deformation contingent on both space and time. In-plane motion is neglected. The velocity of dm is

$$\vec{R} = \vec{\Omega} \times \vec{R} + \vec{r}_2 \tag{4}$$

We determine the kinetic and potential energy of dm and integrate them over the wing's mass and volumetric domains, respectively, such that the total kinetic energy T and potential energy U are

$$T = \frac{1}{2} \int_{m} \vec{R} \cdot \vec{R} dm \tag{5}$$

$$U = \frac{1}{2} \int_{V} \hat{S}(W, W) dV \tag{6}$$

where  $\hat{S}$  is a symmetric, quadratic strain energy density function. Next, we discretize the elastic deformation into an infinite series of space-dependent mode shapes  $\phi_k(\vec{r_1})$  multiplied by time-dependent modal responses  $q_k(t)$  such that

$$W(\vec{r}_1, t) = \sum_{k=1}^{\infty} \phi_k(\vec{r}_1) q_k(t)$$
 (7)

Vibration mode shapes are normalized with respect to the wing mass to satisfy the following orthonormal conditions:

$$\int_{m} \phi_{k} \phi_{r} dm = \delta_{kr} \tag{8}$$

$$\int_{V} \hat{S}(\phi_k, \phi_r) dV = \omega_k^2 \delta_{kr} \tag{9}$$

where  $\omega_k$  is the wing's kth natural frequency and  $\delta_{kr}$  is the Kronecker delta. We define two vector quantities  $\vec{a}_k$  and  $\vec{b}_k$ .  $\vec{a}_k$  is a weighted vector directed from the fixed origin of the rotating frame to the inertial force center of the kth vibration mode, and  $\vec{b}_k$  is a  $\pi/2$  counter-clockwise rotation of  $\vec{a}_k$ . These vectors are

$$\vec{a}_k = \int_m \phi_k(x\vec{e}_x + y\vec{e}_y)dm \tag{10}$$

$$\vec{b}_k = \int_{\mathbb{R}} \phi_k(-y\vec{e}_x + x\vec{e}_y)dm \tag{11}$$

Using these definitions, we write the canonical definitions of kinetic and potential energy (Eqs. (5) and (6)) as

$$T = \frac{1}{2} \vec{\Omega}^T \mathbf{I}_0 \vec{\Omega} + \frac{1}{2} (\Omega_x^2 + \Omega_y^2) \sum_{k=1}^{\infty} q_k^2$$

$$+ \frac{1}{2} \sum_{k=1}^{\infty} \dot{q}_k^2 - \Omega_z \vec{\Omega} \cdot \sum_{k=1}^{\infty} \vec{a}_k q_k - \vec{\Omega} \cdot \sum_{k=1}^{\infty} \vec{b}_k \dot{q}_k$$
(12)

$$U = \frac{1}{2} \sum_{k=1}^{\infty} \omega_k^2 q_k^2$$
 (13)

where  $I_0$  is the inertial tensor of the wing with respect to the reference frame origin. For a flat wing of negligible thickness,  $I_0$  is

$$\mathbf{I}_{0} = \int_{m} \begin{bmatrix} y^{2} & -xy & 0 \\ -xy & x^{2} & 0 \\ 0 & 0 & x^{2} + y^{2} \end{bmatrix}, \quad dm = \begin{bmatrix} I_{xx} & I_{xy} & 0 \\ I_{xy} & I_{yy} & 0 \\ 0 & 0 & I_{zz} \end{bmatrix}$$

where  $I_{xx}$ ,  $I_{yy}$ , and  $I_{zz}$  are the moments of inertia about the x, y, and z axes, respectively, and  $I_{xy}$  is the x-y product of inertia. Prior to formulating the Lagrangian and determining the equation of motion governing  $q_k$ , we account for the nonconservative forces acting on the wing surface. Given that in-plane deformation is neglected, we consider only aerodynamic forces normal to the wing surface  $F_N$ . We incorporate the physical aerodynamic force into the modal equation of motion using the principle of virtual work. The virtual work  $\delta \mathcal{W}$  done by the aerodynamic force is

$$\delta \mathcal{W} = \int_{S} F_{N}(\vec{r}_{1}, t) \delta W(\vec{r}_{1}, t) dS_{w}$$
 (14)

$$\delta \mathcal{W} = \int_{S_w} F_N(\vec{r}_1, t) \sum_{k=1}^{\infty} \phi_k(\vec{r}_1) \delta q_k(t) dS_w$$
 (15)

where  $S_w$  is the surface area of the wing. The nonconservative generalized force  $Q_k$  corresponding to the  $q_k$  degree-of-freedom is

$$Q_{k} = \int_{S_{w}} F_{N}(\vec{r}_{1}, t) \phi_{k}(\vec{r}_{1}) dS_{w}$$
 (16)

With each modal excitation known, we now determine the equation of motion governing generalized coordinate  $q_k$  using the Lagrangian formulation. For  $q_k$ , the general form of Lagrange's equation is

$$\frac{d}{dt} \left( \frac{\partial T}{\partial \dot{q}_k} \right) - \frac{\partial T}{\partial q_k} + \frac{\partial U}{\partial q_k} = Q_k \tag{17}$$

After substituting the explicit forms of T and U (Eqs. (12) and (13)) into Eq. (17), the equation of motion for  $q_k$  is

$$\ddot{q}_k + [\omega_k^2 - (\Omega_x^2 + \Omega_y^2)]q_k = \dot{\vec{\Omega}} \cdot \vec{b_k} - \Omega_z \vec{\Omega} \cdot \vec{a_k} + Q_k$$
 (18)

The equation of motion is linear and time-varying, where the time variance occurs in the stiffness term due to centrifugal softening. The modal excitation terms to the right-hand side of the equation

**Journal of Vibration and Acoustics** 

DECEMBER 2019, Vol. 141 / 061002-3

correspond to the Euler force, centrifugal force, and aerodynamic force, respectively.

The advantage of this model resides with its generality. It can accommodate any flapping wing for which mode shape and natural frequency data are available. Both quantities can be determined experimentally or through numerical methods such as static FEA. Moreover, this framework can accommodate any fluid loading scheme, ranging from low-fidelity BET approaches to higher-fidelity CFD. It can account for unilateral coupling or bilateral coupling. In the former, the fluid affects the structure but not vice versa, and in the latter, the structural and fluid physics are solved simultaneously. In the sections that follow, we demonstrate the utility of our model investigating a simulated *M. sexta* insect wing.

**2.2 Fluid Modeling.** To determine the aerodynamic modal forces  $Q_k$ , we must first identify the physical aerodynamic force  $F_N$ . We consider two fluid modeling approaches in this work: BET and RANS CFD. BET is a reduced-order quasistatic method that approximates aerodynamic forces quickly; however, the method relies on empirical coefficients and lacks the quantitative accuracy of higher-fidelity approaches. RANS is the gold standard for flapping wing fluid dynamics, though the appreciable computational resources required to generate CFD solutions renders this method undesirable for parametric studies. These two fluid dynamics models are detailed in Secs. 2.2.1 and 2.2.2.

2.2.1 Blade Element Theory. Quasi-steady BET is used frequently in the study of insect flight and is useful for reduced-order modeling of wings with high aspect ratios. There are numerous formulations based upon BET which range from relatively basic to reasonably complex [19,21,23]. While BET cannot model certain dynamic phenomena such as clap-and-fling, wing-wake interactions, or dynamic stall that are important to the flight dynamics of many flapping wing fliers [30,31], it does provide order-of-magnitude estimates of aerodynamic forces and moments at substantially lower computational costs compared to direct fluid solvers such as RANS CFD. BET is most suitable for coarse parameter studies where absolute quantitative accuracy is not essential and where high-order fluid solvers are prohibitive. Once approximate solution trends have been identified via BET, high-fidelity CFD can be used to verify the accuracy of BET for parameter sets of interest. This verification will indicate whether or not dynamic effects unaccounted for by the BET formulation will significantly alter aerodynamic loading. In this work, we aim to identify a range over which BET approximates aerodynamic modal forces reasonably well compared to those determined via RANS CFD. We implement a very basic form of the BET framework to illustrate how well a crude fluid loading model performs relative to a higherfidelity method. The BET formulation used hereafter originated in Ref. [22] and is summarized here for clarity. This previous work treated the wing as rigid and did not consider FSI.

The BET method partitions the wing into chord-wise strips called blade elements (Fig. 2). Each blade element is treated as an airfoil with constant depth. Assuming the aerodynamic coefficients and velocity of each blade element are known, the elemental aerodynamic forces can be calculated and integrated over the wing surface to yield the total forces. In general, the scalar differential force *dF* acting on a blade element is

$$dF_{[\cdot]} = \frac{1}{2} C_{[\cdot]} \rho_f \vec{V} \cdot \vec{V} dS_w$$
 (19)

where  $(1/2)\rho_f \vec{V} \cdot \vec{V}$  is the dynamic pressure,  $\rho_f$  is the fluid density,  $\vec{V}$  is the relative velocity between the blade element and the air, C is an arbitrary aerodynamic coefficient, and  $dS_w$  is the differential surface area of the blade element, defined by the chord-width c(r) multiplied by the differential length dr.  $[\cdot]$  denotes a placeholder for lift (L) or drag (D). The velocity of a blade element is assumed constant across that element with respect to a reference point r on the wing, where r is coincident with the y axis. We choose

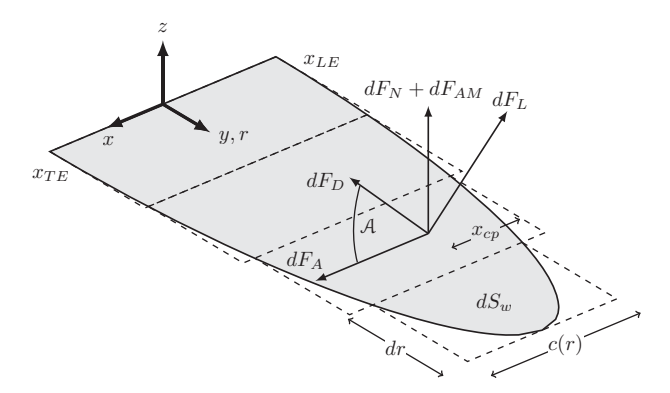


Fig. 2 Blade-element discretization of a wing. Differential aero-dynamic forces shown acting at the center of pressure  $x_c p$  for a single element.

pitching axis as the velocity reference line to be consistent with other flapping wing BET models [20,23]. Because we assume hovering flight, the freestream air velocity is equal in magnitude and opposite in direction of the velocity of the element. The lift and drag coefficients to be substituted into Eq. (19) are

$$C_L(\mathcal{A}) = C_{L, \max} \sin(2\mathcal{A})$$
 (20)

$$C_D(A) = \left(\frac{C_{D, \text{max}} + C_{D,0}}{2}\right) - \left(\frac{C_{D, \text{max}} - C_{D,0}}{2}\right)\cos(2A)$$
 (21)

where  $C_{L,\max}$ ,  $C_{D,\max}$ , and  $C_{D,0}$  are empirically measured coefficients. The aerodynamic angle of attack  $\mathcal{A}$  is defined as the clockwise angle between  $\vec{V}$  and the x axis, or

$$\mathcal{A} = \tan^{-1} \left( \frac{\vec{V} \cdot \vec{e_z}}{\vec{V} \cdot \vec{e_x}} \right) \tag{22}$$

Lift and drag forces are projected onto the wing's axial and normal directions by a simple rotation of  $\mathcal A$  such that

$$dF_A = dF_D \cos A - dF_L \sin A \tag{23}$$

$$dF_N = dF_D \sin A + dF_L \cos A \tag{24}$$

Next, we account for added mass. Insect wings are extremely lightweight and have a large surface area; as a result, added mass cannot safely be neglected. The normal component of added mass acting on a blade element is

$$dF_{AM} = -\frac{\pi}{4}\rho_f c(r)r[\dot{\Omega}_x + \Omega_y \Omega_z]dS + \frac{\pi}{8}\rho_f c(r)^2 [c(r) + 2x_{\text{TE}}(r)]\dot{\Omega}_y dr$$
(25)

This expression for added mass originated from Ref. [32] has been modified as per the reference frame and kinematics used in this work. We assume that the elemental aerodynamic forces act on the elemental center of pressure  $x_{cp}(r)$ . We estimate the location of  $x_{cp}$  using an approximate form of the empirical relationship in Ref. [23] as

$$x_{cp} = x_{LE}(r) + \frac{1}{4}c(r)|\mathcal{A}|$$
 (26)

where  $x_{\rm LE}$  is the wing's leading edge. Note that the aerodynamic force acts at a single discrete point within an element, whereas in reality, aerodynamic pressure acts over the entire wing surface. We stress that BET is subject to the assumptions that underlie thin airfoil theory. Without modification, BET is not well suited to account for large angles of attack or certain phenomena such as dynamic stall. These assumptions may limit the parameter space where BET provides good estimates of aerodynamic forces.

2.2.2 Reynolds-averaged Navier–Stokes Computational Fluid Dynamics. RANS is one of the most widely used formulations of the Navier–Stokes equations to simulate problems involving turbulent fluid flow. Instead of solving for the instantaneous velocity and pressure, RANS separates these variables into their mean  $\langle [\,\cdot\,] \rangle$  and perturbed  $[\,\cdot\,]'$  parts. Taking the average of the incompressible form of the equations results in conservation of mass

$$\frac{\partial \langle u_i \rangle}{\partial x_i} = 0 \tag{27}$$

and conservation of momentum

$$\rho_f \frac{\partial \langle u_i \rangle}{\partial t} + \rho_f \frac{\partial}{\partial x_i} \left( \langle u_i \rangle \langle u_j \rangle \right) = \frac{\partial P}{\partial x_i} + \mu \nabla^2 \langle u_i \rangle - \frac{\partial \tau_{ij}}{\partial x_j}$$
(28)

where  $u_i$  is a component of fluid velocity, P is the pressure,  $\mu$  is the dynamic viscosity, and  $\tau_{ij} = \rho_f \langle u_i' u_j' \rangle$  is the Reynolds stress tensor [33]. While the Navier–Stokes equations are largely unchanged and permit a direct calculation of the mean velocity and pressure fields, the perturbed velocities remain within the stress tensor and require additional equations to model. The closure of the RANS equations has resulted in numerous turbulence models that facilitate, though are often insufficient approximations, modeling flow separation near walls.

The eddy viscosity hypothesis relies on assuming turbulence, and momentum diffusion operates under similar mechanisms [33]. This results in the Reynolds stress tensor being a function of a modeled viscosity and the kinetic energy of turbulent fluctuations, k, such that

$$\tau_{ij} = -\mu_t \left( \frac{\partial \langle u_i \rangle}{\partial x_j} + \frac{\partial \langle u_j \rangle}{\partial x_i} \right) + \frac{2}{3} \rho_f \delta_{ij} k \tag{29}$$

where  $\delta_{ij}$  is the Kronecker delta tensor. The Spalart–Allmaras model is a one-equation model for turbulence closure that solves the transport of a modified diffusivity, which is then used to calculate the eddy viscosity  $\mu_t$  [34,35]. The Spalart–Allmaras model allows for a compromise between computational efficiency and the difficulty most turbulence models have at capturing flow separation near a wall in highly dynamic systems.

A chimera meshing approach is adopted to account for the large body motions [36]. Unlike small body motions within a CFD simulation that shift surface nodes (and their neighbors to avoid creating negative-volume elements), large body motions often rely on remeshing significant portions of the entire domain. The added computational cost of regenerating a mesh and interpolating solution variables between these grids at each time step does not, however, guarantee that a mesh of sufficient quality is maintained. Alternatively, multiple high-quality meshes for the fluid domain empty of any boundaries (the background mesh) and a region surrounding the moving wing (the *overset* mesh) can be overlapped. These meshes remain unchanged throughout the simulation, with the overset mesh undergoing rigid body motion following the wing. At each time step, the region of overlap is determined and an enveloping shell of elements near the boundary of the overset mesh is used to interpolate between the solution in each region. A distance-weighted interpolation is used to couple the background and overset meshes into a strongly coupled system of equations.

 $dF_A$ ,  $dF_N$ , and  $x_{cp}$  are easily queried from the time-varying mean velocity and pressure fields on the upper and lower surfaces of the wing. The component values of wall shear stress and pressure are transformed onto the wing reference frame and summed along chordwise and spanwise segments in order to match the desired resolution of the BET model. The Spalart–Allmaras RANS model with chimera grid within STAR-CCM+ v12.04 was used to produce the CFD results in this work.

### 3 Simulation

In this section, we apply the derived model to a fictitious hawkmoth *M. sexta* wing. We begin the section by describing all simulation parameters. We then (1) compare physical and modal aerodynamic forces predicted by BET and CFD, (2) assess the sensitivity of BET-estimated modal forces with respect to flapping kinematics, (3) compare inertial-elastic to aerodynamic modal forces, and (4) solve for the wing's response in air and in vacuum.

**3.1 Simulation Parameters.** We first identify the parameters necessary to carry out the simulation. All parameters are shown in Table 1. We develop an idealized model of a hawkmoth M. sexta wing using ABAOUS FEA. An image of the forewing is digitally traced to determine the to-scale wing planform. We assume that the wing has constant thickness and density. The values of these properties are estimated from Ref. [37]. Venation, camber, and spatial thickness variation are neglected. The FEA model is composed of 611 shell elements, which is a sufficient number of elements to show convergence of the wing's first two natural frequencies (Fig. 4). We retain the two vibration modes corresponding to these natural frequencies. The first is a bending mode and the second is a torsional mode (Fig. 3). Because of the geometric and structural simplifications of the FEA model, the natural frequencies of the wing had to be adjusted in postprocessing to agree with experimentally reported values [38] shown in Table 1. The first two inertial force center vectors are  $\vec{a}_1 = -(0.57\vec{e}_x + 2.0\vec{e}_y) \times 10^{-4}$ and  $\vec{a}_2 = -(0.42\vec{e}_x + 0.06\vec{e}_y) \times 10^{-4}$  in units kg/m<sup>2</sup>.

Next, we discuss the parameters used for fluid modeling. For the CFD simulations, the wing is represented as an embedded surface within the overset mesh region. The simulation geometry is shown in Fig. 5. A prism layer was introduced to improve the boundary layer representation of the wing. A time step was specified to capture approximately 10 deg of wing rotation and a total of 10 rotation periods were simulated to reach a periodically steady response. Axial and normal forces for every surface element were exported at each time step. CFD parameters are summarized in Table 2. We conduct a mesh independent study that scaled the mesh size and maintained the relative size ratios throughout the simulation space. A mesh of nearly 2 million elements was considered converged, resulting in a root mean square error of 1.5% (with respect to the maximum force value) and an error of 2.5% for a grid of 442,595 elements. A time-step independence study was performed for the selected grid, and convergence was found at a time-step of  $1.25 \times 10^{-4}$  s (1.25 deg/time-step). This resulted in a root mean square error of 4% (with respect to the maximum force value) and a maximum peak error of 7.2% at a time-step of  $1.0 \times$ 10<sup>-3</sup> s. While the selected time-step only results in 40 points per cycle, it was deemed to adequately capture the first-order forces and their profile within the scope of this paper and with tractable

Table 1 Structural, geometric, and aerodynamic simulation parameters

Variable	Description	Value	Unit
$\omega_1$	First natural frequency	59	Hz
$\omega_2$	Second natural frequency	75 47	Hz mg
$m_w$	Wing mass		
$C_{L,\max}$	Max lift coefficient	1.68	_
$C_{D,\max}$	Max drag coefficient	3.06	_
$C_{D,\min}$	Min drag coefficient	0.07	_
R	Wing span	54	mm
AR	Aspect ratio	3.48	
A	Surface area	867	$mm^2$
$\bar{c}$	Mean chord width	15.5	mm
$\rho_f$	Fluid density	1.2	kg/m <sup>3</sup>
t	Thickness	45	μm
$\rho_w$	Wing density		kg/m <sup>3</sup>

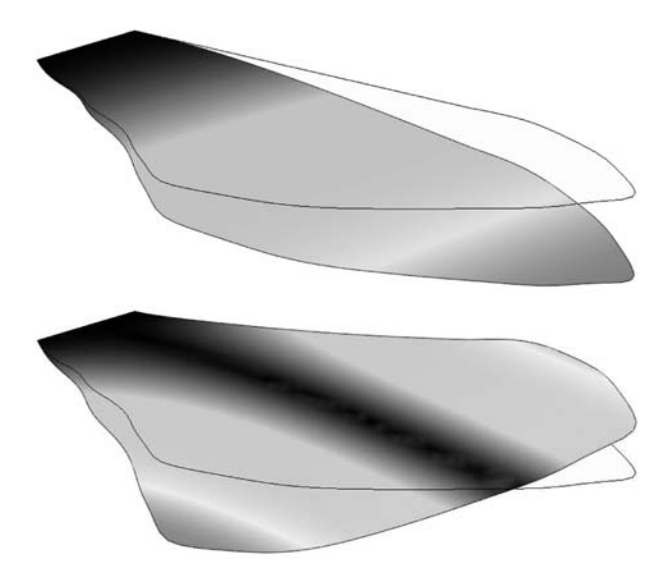


Fig. 3 First two vibration modes of model hawkmoth forewing. (Top) Spanwise bending mode and (bottom) spanwise torsion mode.

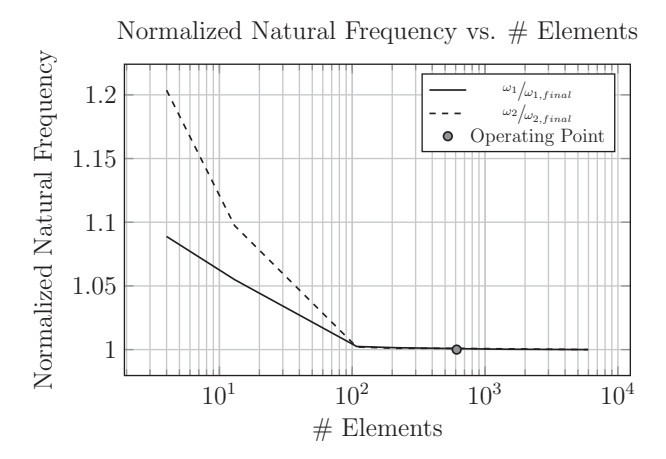


Fig. 4 Convergence study of the FEA model. The first and second natural frequencies normalized by their final values are plotted with respect to number of elements. We use 611 elements for the simulations carried out in this work.

computational times. Phase relationships were determined to be independent of the time step and mesh fineness.

For BET simulations, we discretize the wing into 20 blade elements. This number of elements showed convergence for lift averaged over a single wingbeat. The aerodynamic coefficients are taken from values reported in Ref. [21] for the hawkmoth. BET simulations are conducted numerically using MATLAB. All simulations occur over 25 wingbeats, where each wingbeat is divided into 100 equally spaced time intervals. Because CFD simulations occur on a much coarser time scale, all CFD results are interpolated in time to match the finer MATLAB time scale. All physical aerodynamic forces determined either via CFD or BET are transformed to modal aerodynamic forces through Eq. (16).

When solving for the wing modal responses, we introduce light modal damping ( $\zeta = 0.05$ ) into both modes to attenuate the wing's free vibration. Results presented hereafter are taken once steady-state dynamics have been achieved. For frequency domain calculations, we use MATLAB's curve fitting toolbox to identify Fourier series coefficients and calculate signal magnitude and phase from these coefficients. All flapping kinematics are idealized as harmonic and of the form  $\eta = \eta_0 \sin{(\omega t + \phi_\eta)}$ , where  $\eta$  is a general

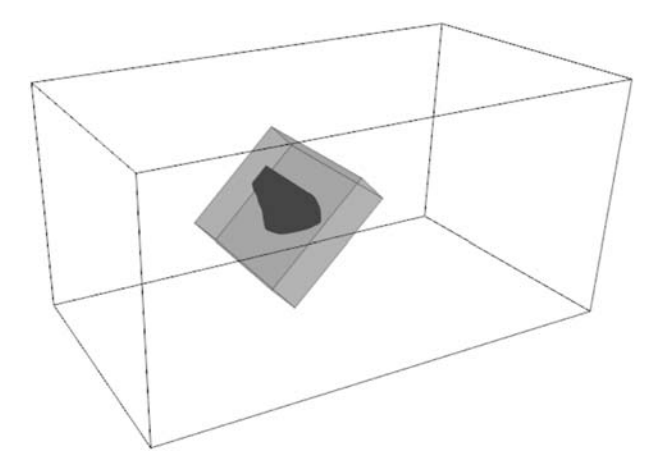


Fig. 5 CFD simulation geometry showing the background region (outline), overset region (shaded), and wing

Table 2 CFD simulation parameters

Variable	Description	Value	Unit
μ	Dynamic viscosity of air	$1.85 \times 10^{-5}$	Pa·s
$\Delta t$	Time step	0.001	S
$t_f$	Simulation time	0.4	S
	Dimensions of the background mesh $(L \times W \times H)$	$200 \times 110 \times 100$	mm
	Mean element length of the background mesh	1.0	mm
	Number of elements in the background mesh	326,538	_
	Dimensions of the overset mesh $(L \times W \times H)$	$55 \times 70 \times 15$	mm
	Mean element length of the overset mesh	0.5	mm
	Mean element length of the wing surface	0.125	mm
	Number of prism layers off the wing	5 –	
	Prism layer growth rate	1.2	_
	Number of elements in the overset mesh	116,057	_
<del>y</del> <sup>+</sup>	Mean <i>y</i> -plus for one period of rotation	3.763	_

Table 3 Kinematic parameters for hovering flight

Variable	Description	Value	Unit
$\alpha_0$	Roll amplitude	60	deg
$\beta_0$	Pitch amplitude	45	deg
γο	Yaw amplitude	0	deg
$\phi_{lphaeta}$	Pitch/roll phase difference	$\pi/2$	rad
ω	Flap frequency	25	Hz

rotation function that represents roll, pitch, or yaw,  $\eta_0$  is the rotation amplitude,  $\omega$  is the flapping frequency, and  $\phi_\eta$  is the rotation phase. We consider only hovering flight in this work. We estimate flapping kinematics from Ref. [39], including pitch/roll rotation amplitudes, rotation phase, and flap frequency. We neglect wing yaw which is typically small in insect flight [39]. All kinematic parameters for hovering flight are shown in Table 3.

**3.2** Physical and Modal Aerodynamic Forces. We begin by comparing the net aerodynamic normal force  $F_N$  calculated via BET and CFD. This comparison provides a baseline accuracy for the

Aerodynamic Normal Force vs. Wingbeat Fraction

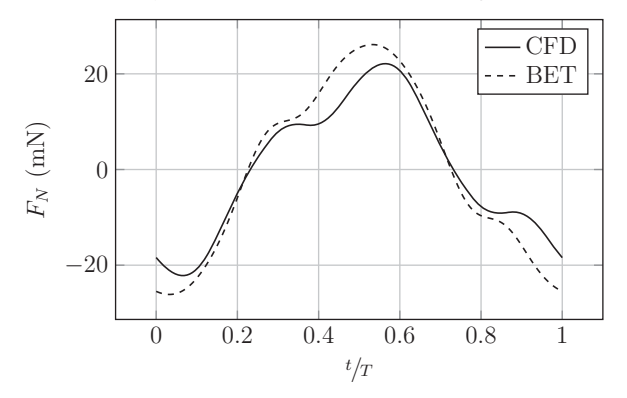


Fig. 6 Aerodynamic normal forces calculated via BET and CFD

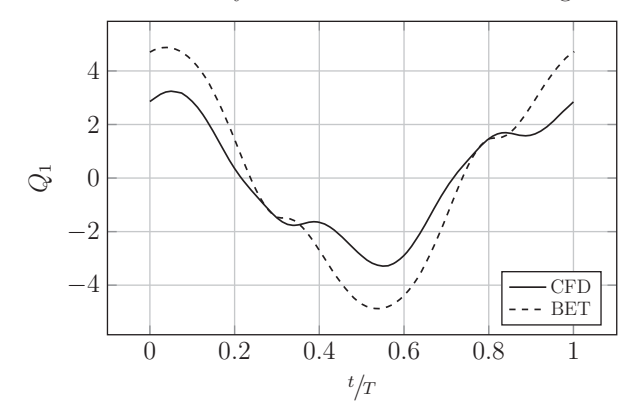
BET method. If BET cannot estimate bulk aerodynamic forces within reasonable accuracy, it will be unable to estimate aerodynamic modal forces. In this case, we treat CFD as the ground truth. We calculate  $F_N$  using both methods and plot it as a function of wingbeat fraction t/T in Fig. 6.

Both fluid models indicate that  $F_N$  oscillates primarily at the driving frequency  $\omega$  with a notable harmonic at  $3\omega$ . Overall, we see good agreement between CFD and BET both in magnitude and phase. Most notably, BET overestimates the primary response magnitude by approximately 30%. This discrepancy is likely due to aerodynamic coefficient constants as well as the idealized relationship between the aerodynamic coefficients and angle of attack (Eqs. (20) and (21)). In general, insect wings will deviate modestly in size and geometry; it is unlikely that a universal set of aerodynamic coefficients exits. Thus, BET is capable of estimating net aerodynamic forces for hovering flapping kinematics with reasonable agreement to CFD. Quantitative accuracy of the BET method is contingent on precise empirical aerodynamic coefficients.

Next, we consider aerodynamic modal forces  $Q_1$  and  $Q_2$ . Aerodynamic modal forces are calculated via Eq. (16). For the CFD model, the spatial distribution of aerodynamic forces is known. Conversely, for the BET model, we know only the net force on each blade element and do not know the force distribution. We assume that the elemental aerodynamic normal force acts as a point load at the blade elements center of pressure. Aerodynamic modal forces calculated via CFD and BET are plotted in Fig. 7. The corresponding numeric values are shown in Table 4.

From this comparison, we see modal forces calculated via BET which agree qualitatively with those calculated via CFD. BET accurately predicts the frequency components as well as the phase of these components. In addition, BET agrees with CFD quantitatively for the second aerodynamic modal force  $Q_2$ . The  $\omega$  components are nearly identical in magnitude and phase, and the  $3\omega$  components agree in magnitude. There is a slight discrepancy in the phase at  $3\omega$ . We observe that the BET-predicted second modal force is not as smooth as that predicted by CFD. This stems from the point load approximation used for the BET model. When the center of pressure crosses over the nodal line of the torsional mode (Fig. 3), the force contribution of that particular blade element to the modal response is effectively negated. In reality, there would be some force distribution about this center of pressure that would generate a smoother second modal force. However, this force distribution is unknown if the pressure coefficients  $c_p$  over the range of angles of attack for a blade element are unknown. Then, the nonsmooth behavior arising from the point-load approximation could introduce anomalous high-frequency components into  $Q_2$ , though these components likely do not affect the second modal response given that they will occur at frequencies much higher than the second natural frequency. Thus, even with the point load approximation, BET predicts the second modal response fairly well.

First Aerodynamic Modal Force vs. Wingbeat



Second Aerodynamic Modal Force vs. Wingbeat

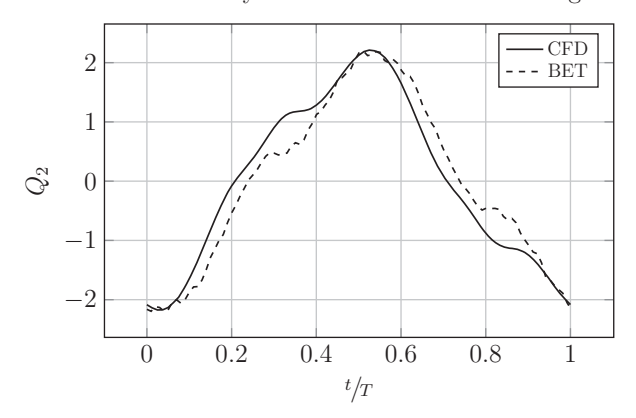


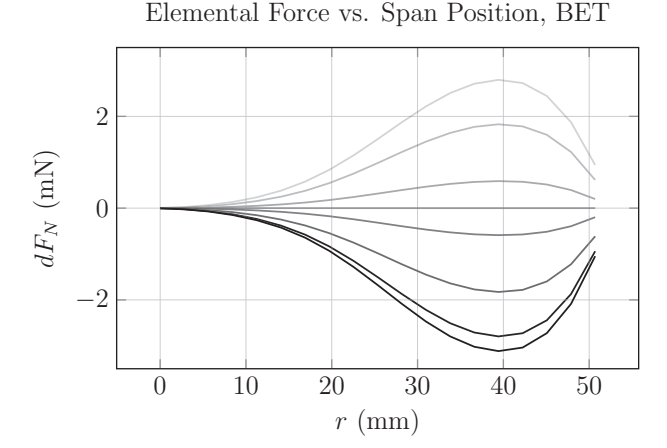
Fig. 7 Aerodynamic modal forces calculated via CFD and BET

Table 4 Numerical comparison between first and second aerodynamic modal forces estimated by BET and CFD for hovering flapping kinematics

	BET	CFD	BET	CFD
	$Q_1$	$Q_1$	$Q_2$	$Q_2$
$ \omega $	4.52	2.84	1.92	1.91
$ 3\omega $	0.67	0.69	0.34	0.35
$\angle \omega$ (rad)	0.08	-0.04	3.25	3.03
$\angle 3\omega$ (rad)	1.34	1.6	4.21	4.23
$ \omega $ % diff.	58.9		0.26	
$ 3\omega $ % diff.	3.4		3.2	
$\Delta \angle \omega$ (rad)	-0.12		-0.22	
$\Delta 3 \angle \omega$ (rad)	0.27		0.02	

On the other hand, the discrepancy between CFD and BET estimates of  $Q_1$  is larger. BET overestimates the primary response magnitude of  $Q_1$  by approximately 50%. This suggests that BET predicts the spanwise location of the aerodynamic force center further along the r axis than CFD does. To verify this, we plot the time history of the elemental force  $dF_N$  as a function of blade element position r for both CFD and BET models. Results are shown in Fig. 8. Note that the spanwise aerodynamic force center moves along r over time with the CFD model and is stationary with the BET model. CFD predicts the time-averaged spanwise location of the aerodynamic force at  $r \approx 3.52$  cm, whereas BET predicts it at  $r \approx 3.94$  cm. Because the first bending mode (Fig. 3) varies approximately quadratically along the r axis, even a small increase in the spanwise position of the aerodynamic force center significantly affects the first modal force.

Thus, it appears that BET can only crudely estimate the position of the aerodynamic force center. We believe that this is in part



Elemental Force vs. Span Position, CFD

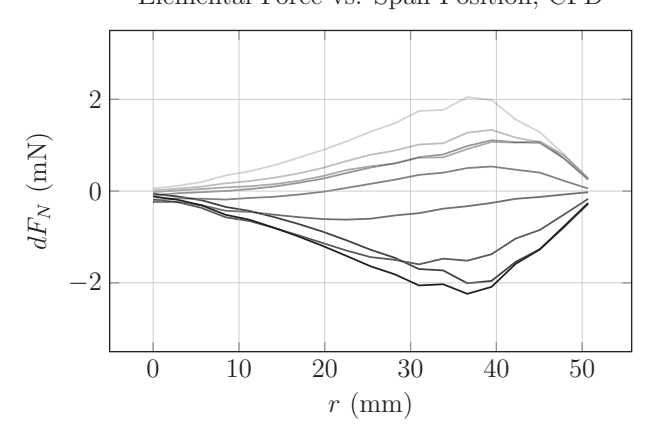


Fig. 8 Elemental aerodynamic normal force  $dF_N$  as a function of spanwise position r for both CFD and BET models. Time history shown over a half wingbeat. Dark lines indicate the beginning of the half wingbeat, and lighter lines indicate the end of the half wingbeat.

because BET is not well suited to account for rotational forces. By convention, the blade element velocity is referenced from a line coincident with the y axis (Fig. 2). This implies that if a wing is undergoing pure pitch about the y axis, BET predicts no aerodynamic forces acting on the wing except for those imparted by added mass. Consequently, at least some forces associated with dynamic pitching are not accounted for simply because of the velocity reference line r. However, other rotational forces must be considered to improve the BET formulation as well. For example, Kramer observed that rapid changes in an airfoils angle of attack lead to short spikes in lift force [40]. He conjectured that these spikes were associated with flow separation, where the fluid becomes detached from the surface of an object. Given that an insect wing changes angles of attack rapidly, these dynamic factors may play a nontrivial role in aerodynamic loading. While rotational terms have been incorporated into BET [18,23,41], most are case-specific and cannot be applied with generality. We were unable to incorporate rotational terms into our BET model that reduced the difference between BET and RANS estimated modal forces for all parameters considered in the sensitivity study that follows (Fig. 9). Whitney and Wood used the BET method to estimate the aerodynamic forces of a small flapping wing robot and were also unable to improve model-theory agreement by incorporating a rotational lift term [23]. Sane and Dickinson suggest that rotational coefficients are sensitive to the location of the pitching axis as well as pitching rate and amplitude [18], which makes it difficult to model as a quasi-steady force without sufficient empirical data.

Despite the limitations of BET, it remains a useful tool that provides reasonable estimates of modal forces at significantly reduced computational costs relative to CFD. In this case, BET predicts modal forces staggering five orders-of-magnitude faster than CFD. This enormous reduction in computational time can expedite parametric studies considering wing geometry, mass/stiffness distributions, and flapping kinematics. However, up to this point, we have considered only hovering flight flapping kinematics. It is possible that the BET model breaks down for deviations from these kinematics

**3.3** Sensitivity of Blade Element Theory. In Sec. 3.2, we saw that BET predicted the first and second aerodynamic modal forces reasonably well for hovering flapping kinematics. In this section, we explore how deviations from hovering flapping kinematics affect the agreement between CFD and BET calculated modal forces. Pohly et al. compared BET and CFD fluid models for various flapping kinematics [42]; however, this study focused on how well BET estimates bulk aerodynamic forces (e.g., net lift and thrust) for rigid wings. To estimate the range of parameters over which BET can be used to model FSI, it is more suitable to compare aerodynamic modal forces rather than bulk aerodynamic forces.

For our sensitivity analysis, we consider four kinematic parameters; roll amplitude  $\alpha_0$ , pitch amplitude  $\beta_0$ , phase difference between pitch and roll  $\phi_{\alpha\beta}$ , and driving frequency  $\omega$ . Starting from their nominal value in hovering flight (Table 3), we vary each rotation parameter from  $\pm \pi/8$  in  $\pi/16$  increments. We also consider driving frequencies of 15, 25, and 35 Hz for normal hovering kinematics. We do not consider simultaneous variation of parameters because of how computationally demanding CFD solutions are. Nonetheless, varying parameters individually provides a good initial picture of how well BET estimates modal forces under different scenarios.

For each set of parameters, we calculate the first and second aerodynamic modal forces  $Q_1$  and  $Q_2$  via both BET and CFD. Because the modal forces oscillate both at the driving frequency and three times the frequency, we must determine the magnitude and phase at both  $\omega$  and  $3\omega$ . Across all parameters tested, we did not identify any other significant frequency components. We then determine the percent error between the modal force magnitude at each frequency component assuming that CFD provides the "true" solution. We also identify the phase differences at  $\omega$  and  $3\omega$  between CFD and BET modal forces. These calculations are tabulated numerically in Table 4 as an example for hovering flapping kinematics. The percent error and phase difference for deviations from hover kinematics are plotted in Fig. 9.

Overall, BET estimates modal forces reasonably well in both magnitude and phase for modest deviations from hovering flight kinematics. The magnitude error and phase difference of both  $\omega$ and  $3\omega$  components of  $Q_1$  and  $Q_2$  are fairly insensitive to changes in driving frequency. Small changes  $(\pm \pi/16)$  in rotational kinematic parameters generally had a minor effect on the dominant  $\omega$  component magnitude error and phase difference of  $Q_1$  and  $Q_2$ . The effect of these small changes on the  $3\omega$  components of  $Q_1$ and  $Q_2$  is somewhat more pronounced. For  $Q_1$ , errors in the magnitude and phase of  $3\omega$  components likely do not affect the first modal response significantly. This is because the  $3\omega$  component is much smaller in magnitude than the  $\omega$  component for  $Q_1$ , and the wing's first natural frequency does not fall near  $3\omega$  ( $\omega_1 \approx 59$  Hz). However, the  $3\omega$  errors in magnitude and phase of  $Q_2$  may more substantially affect the second modal response because the wing's second natural frequency is near  $3\omega$  ( $\omega_2 \approx 75$  Hz). Nonetheless, the magnitude error for both  $\omega$  and  $3\omega$  of  $Q_1$  and  $Q_2$  for kinematic deviations of  $\pm \pi/16$  is maximally 125%. This suggests that BET performs fairly well for small kinematic deviations.

We observe more significant errors for larger changes  $(\pm \pi/8)$  in rotational kinematic parameters. Such errors generally occur in the  $3\omega$  components of modal forces. However, the largest errors

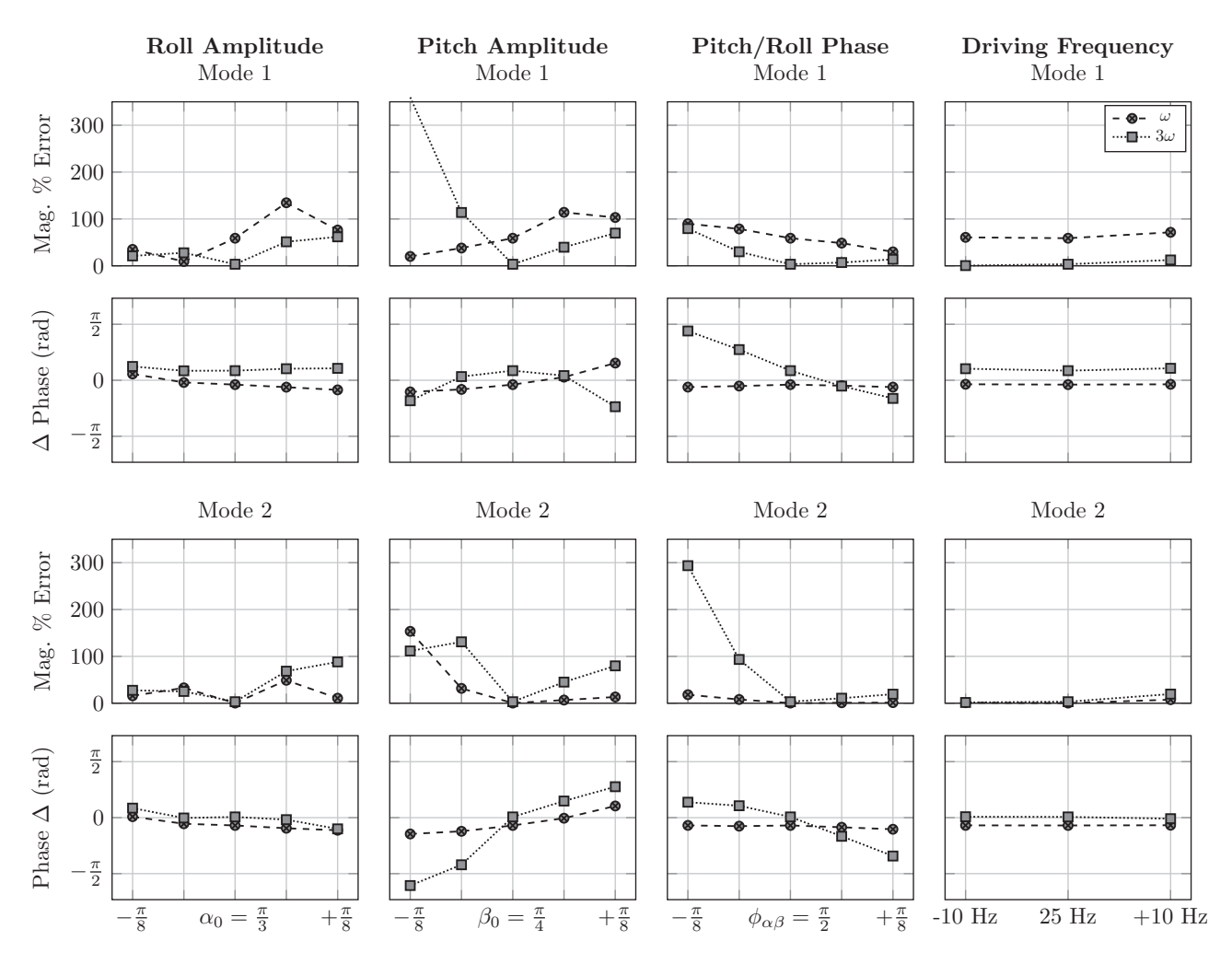


Fig. 9 Sensitivity of BET first and second aerodynamic modal forces as flapping kinematics deviates from hovering flapping kinematics

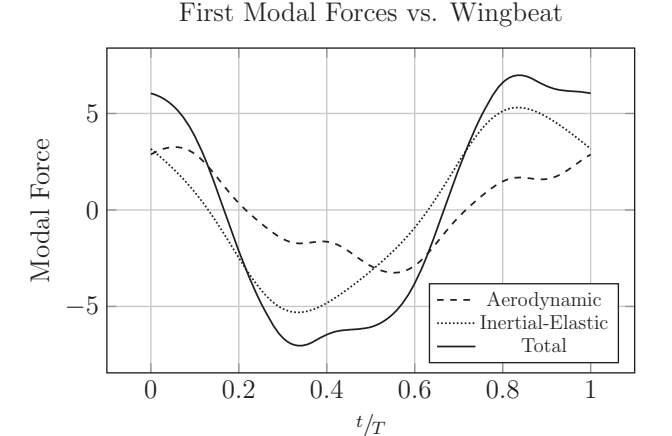
often coincide with flapping kinematics that would not exist in nature. For example, when the pitch amplitude is reduced by  $\pi/8$ , the percent error in the  $3\omega$  component of  $Q_1$  is over 300% and the phase difference for the  $3\omega$  component of  $Q_2$  is roughly  $-\pi/2$ . While these errors are significant, the reality is that if the pitch amplitude were reduced by  $\pi/8$ , the insect would produce far less lift than required to fly. For this pitch amplitude, CFD estimates an averaged vertical force of 12.5 mN whereas a hawkmoth that weights roughly 2.0 g [43] would require closer to 20 mN vertical force to fly. The other most significant errors occur when the pitch/roll phase deviates  $\pm \pi/8$ ; however, these kinematics also produce insufficient vertical force for flight.

It is difficult to identify, with absolute certainty and across all parameters considered, why errors between CFD and BET tend to grow as flapping kinematics deviate from those observed in hovering. However, we believe that away from these nominal kinematics, phenomena that are not modeled by BET become increasingly important to CFD-estimated modal forces. Consider when pitch amplitude is increased by  $\pi/8$ . In this case, the wing undergoes a rotation upon stroke reversal larger than what is typical in hovering. Since rotational affects are not accounted for via BET, we suspect that errors may become greater for increased pitching amplitudes. At the same time, if pitch amplitude is reduced by an equivalent amount, the wing would be nearly vertical and have a very large angle of attack mid-stroke. This poses issues for the classical thin airfoil theory on which BET is based, which is more accurate for small angles of attack because of stall effects at high angles of

attack. Thus, there are many mechanisms that could affect the agreement between CFD and BET away from nominal hovering kinematics, but these mechanisms must be treated on a case by case basis

Despite these differences, the sensitivity analysis also suggests that certain dynamic phenomena unmodeled in BET (e.g., flow separation) only modestly affect its agreement with CFD. Consider the case where roll amplitude is increased from  $\alpha_0 = \pi/3 + \pi/16$  to  $\alpha_0 = \pi/3 + \pi/8$ . CFD shows that the flow is attached to the wing for the lesser roll amplitude, whereas it separates for the greater roll amplitude. But, over this range of roll amplitudes, the maximal magnitude error is 100% and the maximum phase difference is approximately  $\pi/10$  for both  $\omega$  and  $3\omega$  components. This suggests that in some cases, quasi-steady aerodynamic forces are larger than or of similar magnitude to aerodynamic forces imparted by dynamic phenomena. Consequently, BET appears to be a reasonable first approximation of aerodynamic modal forces for flapping kinematics that deviate modestly from those seen in hover.

# **3.4 Inertial-Elastic Versus Aerodynamic Modal Forces and Responses.** We now compare inertial-elastic modal forces to aerodynamic modal forces. This comparison provides insight into which physical regime dominates wing deformation in hovering flight conditions. To clarify, both Euler and centrifugal forces (Eq. (18)) are considered inertial-elastic forces. The first and second modal forces are shown in Fig. 10. BET estimated modal forces are omitted from Fig. 10 for clarity.



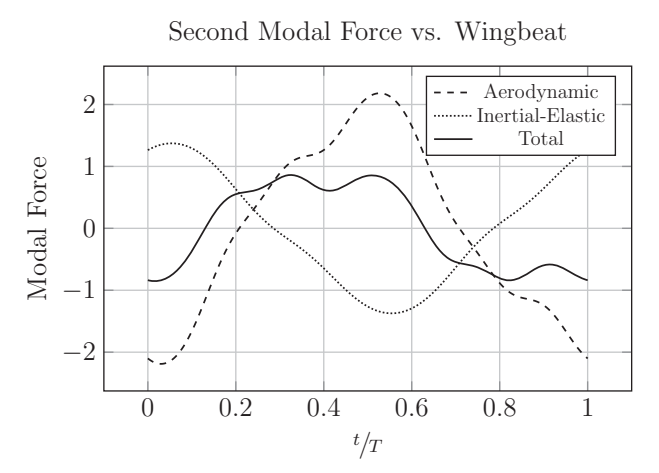
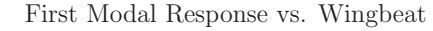


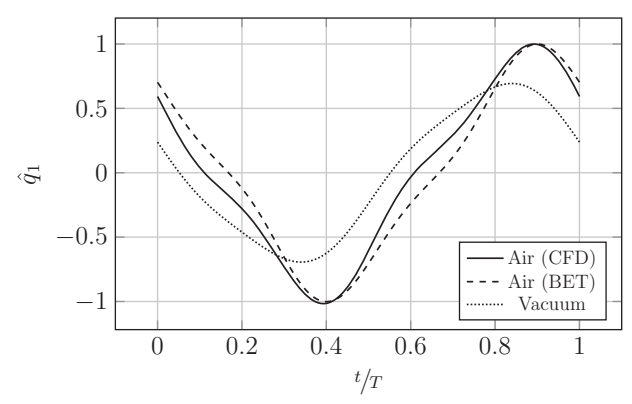
Fig. 10 CFD predicted aerodynamic and inertial-elastic modal forces for first two vibration modes

Overall, inertial-elastic forces are larger than aerodynamic forces for the first vibration mode. Both force types oscillate primarily at  $\omega$  with appreciable components at  $3\omega$ . The magnitude of the primary  $\omega$  component of the inertial-elastic modal force is roughly 1.8 times greater than that of the aerodynamic force. Aerodynamic modal force  $Q_1$  leads the first inertial-elastic modal force by a phase of approximately  $\pi/4$ . As a result, the two components interact constructively and the net modal force is larger than either of the individual parts. The  $3\omega$  magnitude is similar for both aerodynamic and inertial-elastic modal forces and again are out-of-phase by  $\pi/4$ .

For the second vibration mode, aerodynamic forces are larger than inertial-elastic forces. Again, both oscillate at  $\omega$  with a harmonic at  $3\omega$ . The magnitude at  $\omega$  is approximately 1.6 times larger for the aerodynamic force modal force  $Q_2$  compared to the inertial-elastic force. The two forces are out of phase by nearly  $\pi$ . Consequently, the components interact destructively and the net second modal force is smaller in magnitude than the individual aerodynamic or inertial-elastic modal force. The magnitude at  $3\omega$  is approximately three times larger for aerodynamic modal force  $Q_2$  compared to the inertial-elastic modal force. Despite that the net  $3\omega$  magnitude is small for the second modal force, this component is significant given its close proximity to the second natural frequency ( $\omega_2 \approx 75 \, \text{Hz}$ ). We anticipate that this harmonic will dominate the second modal response due to a large gain factor.

Next, we calculate the first and second modal responses for the flapping wing. We consider a wing flapping in air, where both inertial-elastic and aerodynamic forces contribute to deformation, and a wing flapping in vacuum, where only inertial-elastic forces are present. We use both BET and CFD fluid models for the in-air case. This simulation complements the experimental work described in the introduction, where *M. sexta* wings were flapped





Second Modal Response vs. Wingbeat

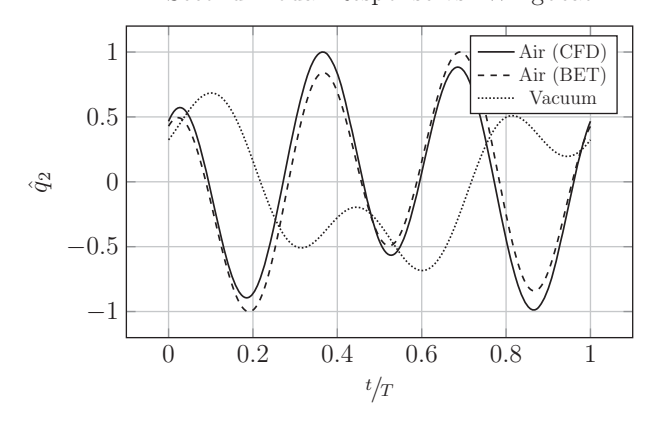


Fig. 11 First two modal responses for flapping in air and in vacuum. Each modal response is normalized with respect to the largest value of the in-air response.

in air and in reduced-density mediums. The notable exception is that we are able to simulate two rotational degrees-of-freedom, whereas these experiments only flapped the wing about the roll axis. We compare the modal responses rather than a physical response (e.g., wingtip deflection), so we can more accurately capture the full-field structural response. Comparing the response of a single point in air and in vacuum can be misleading. Even if that point behaves similarly, other points on the structure may respond differently in the two mediums. We solve the first two modal responses for flapping in air and in vacuum numerically. To verify the accuracy of our numerical results, we developed a closed-form approximate analytic solution (Appendix). The approximate analytic solution agrees well with numerical findings. Numerical results are plotted in Fig. 11, where each modal response is normalized by the largest value in air.

Perhaps most importantly, we see aerodynamic forces contribute significantly to the modal responses and by extension to the wing deformation. This contradicts the findings of Ref. [4], which suggest wing deformation is primarily a function of inertial-elastic forcing. We acknowledge that their work considered only SDOF roll rotation; for SDOF rotation, it is possible that the balance of inertial-elastic and aerodynamic forces is different. However, it is plausible that for SDOF rotation, the contribution of fluid loading to structural deformation would be larger than if a wing was subject to nominal multi-degrees-of-freedom (MDOF) kinematics. If a wing is subject to SDOF rotation, the induced flow is always normal to the wing over the entire flapping cycle. This creates a large pressure over the wing surface. For the MDOF kinematics considered in this work, the wing crosses its mean position oriented at its maximum pitch angle. The wing will be more streamlined with the flow, and as a result, the net fluid load on the wing is less than in

the SDOF case. We conjecture that even for the SDOF case, fluid loading nontrivially affects wing deformation. Indeed, a quick SDOF numerical simulation using the BET fluid model suggests that the first modal response is 25% larger in air than in vacuum.

We now turn our attention to the specific differences between in-air and in-vacuum flapping. In this comparison, we consider only the CFD fluid model. For the first mode, we see the overall peak-to-peak magnitude of the response is roughly 35% smaller in-vacuum than in-air. Like the first modal forces (Fig. 10), the first modal response occurs at the driving frequency and three times the driving frequency. Response magnitude at  $\omega$  is approximately 1.4 times larger in air than in vacuum. Response magnitude at  $3\omega$  is approximately three times larger in air than in vacuum. The phase of the  $\omega$  and  $3\omega$  components is similar in air and in vacuum. While the first modal response  $q_1$  is somewhat similar in air and in vacuum, differences in the second modal response  $q_2$  in air and in vacuum are more distinct. The in-air second modal response occurs primarily at  $3\omega$  with a lesser component at  $\omega$ . The opposite is true for the in-vacuum  $q_2$  response, where the oscillation occurs primarily at  $\omega$  with a lesser component at  $3\omega$ . These trends can be explained by the second modal forces. As indicated by Fig. 10, the second aerodynamic modal response  $Q_2$  has an appreciable component at  $3\omega$ . Because the second natural frequency occurs very close to  $3\omega$ , this modest  $3\omega$  component of  $Q_2$  dominates the response. The second inertial-elastic modal force also has a  $3\omega$  component; however, it is smaller than that of  $Q_2$ . Thus, the in-vacuum response of  $q_2$  is dominated by the  $\omega$  component of the inertial-elastic modal force. Lastly, we note that the phase of oscillation of  $q_2$  is quite different in air and in vacuum. The phase difference between in-air and in-vacuum flapping is nearly  $\pi$  at both  $\omega$  and  $3\omega$  response

Lastly, Fig. 11 shows that the in-air first and second modal responses predicted via BET and CFD are similar. The agreement is particularly good for the first vibration mode, since the inertial-elastic modal force is larger than the aerodynamic modal forces predicted by either fluid model (Fig. 10). Agreement between the second modal responses is also fairly good, though BET predicts a slightly larger  $\omega$  response than CFD. Overall, this comparison further illustrates BET's ability to estimate structural deformation with low computational demands.

## 4 Discussion

Here, we discuss some of the findings of our study and how they are relevant to biological and artificial flapping wing flight. First, we concede that BET is an imperfect method. The formulations most common to flapping wing literature are not well suited to treat dynamic phenomena such as flow separation, wing-wake interactions, or vortex shedding, all of which are observed in some biological fliers [30]. While some researchers have included rotational correction factors into BET formulations [21], we were unable to improve our predictions of aerodynamic modal forces by doing so. Nonetheless, BET with added mass captures some critical aerodynamic loading features required to inform FSI models. This renders BET a powerful tool for parametric design of FWMAV wings. Designers can leverage the framework to identify solution trends and to tailor flapping kinematics, wing mass/stiffness distributions, and geometry. Of course, it is sensible to verify model findings using a higher-fidelity fluid model such as CFD, particularly if unsteady dynamic phenomena are anticipated to play a role in the dynamics. BET should be used primarily to move design solutions into the proximity of an optimal solution and to reduce the parameter design space.

Next, we turn our attention to the physics governing wing deformation. Prior to this work, the relative contribution of inertial-elastic and aerodynamic forces to wing deformation at moth scale was unknown. We believe that both aerodynamic and inertial-elastic forces are on the same order-of-magnitude and as a result, contribute to wing deformation similarly. However, different

forces appear to govern different modes of deformation. For example, inertial-elastic forces are somewhat larger for the bending mode whereas aerodynamic forces are modestly larger for the torsional mode. The implications of different force types governing different modes of deformation may be important.

More evolved insects, such as true flies and bees, have a small club-like appendage called a haltere that devolved from their hindwings [44]. The haltere is a gyroscopic organ that enables insects to identify their angular rates of rotation. Halteres generally sit in clefts between the insect abdomen and thorax and are consequently shielded from aerodynamic forces; haltere dynamics are governed almost entirely by inertia. This decoupling of aerodynamic and inertial-elastic forces is believed to be essential for proper haltere function. How do insects who lack halteres, such as moths and butterflies, receive analogous angular rate feedback? Researchers believe that this feedback stems from deforming mechanoreceptors in the forewing. However, it is unclear how such insects decouple inertial forces from aerodynamic forces. If inertial forces govern some modes of deformation and aerodynamic forces govern others, it may be possible to decouple these force types via careful placement and orientation of mechanoreceptors. Indeed, the campaniform sensilla in insect wings are directionally sensitive and distributed widely over the wing. It is possible that their placement and orientation allow for independent sensing of exogenous forces and internal states, thereby allowing the wing to behave as a large, flexible gyroscope.

However, we acknowledge that our findings were derived assuming unilateral coupling between the fluid and the structure. In practice, wing deformation may be large in some contexts and can indeed influence the surrounding flow field. For our model, if we determine the displacement at all nodes, take the absolute values, and then average them spatially, the maximum "average" timevarying displacement is about 1.2 cm at steady-state, which may considerably affect the flow field. For biological fliers, Nakata and Liu estimated via computational methods that wing flexibility increased peak vertical forces in hovering hawkmoths by approximately 22% [45]. This indicates a change in the flow field as a result of wing deformation. On the other hand, Du and Sun found that for hoverflies, some flow characteristics were insensitive to wing deformation and that flexibility increased averaged lift by only 10% [6]. In this case, it is plausible that the flow field is only modestly affected by deformation and that unilateral coupling between fluid and structure is better justified. Consequently, fluidstructure coupling assumptions must be accounted for on a case-by-case basis, though some dynamic phenomena such as aerodynamic damping will inevitable be absent from a unilaterally coupled model. The unilaterally coupled model detailed in this work can be used in part to identify where bilateral coupling may be required.

## 5 Conclusion

Flapping insect wings deform under both aerodynamic and inertial-elastic forces. However, the FSI that governs wing deformation is not well understood. This is in part because conventional FSI models are very high order. To gain a better understanding of the physics governing flapping wing deformation, we developed a novel FSI framework that is (1) reduced-order in the structural domain, (2) capable of accommodating arbitrary wing geometry, (3) able to consider any fluid loading model, and (4) suitable for describing unilateral or bilateral fluid–structure coupling. We apply this framework to study the FSI of a simulated hawkmoth wing. Through this simulation, we assess the accuracy of a low-order BET fluid model and its applicability to FSI problems. Moreover, we identify the relative contributions of aerodynamic and inertial-elastic forces to wing deformation. Key findings are summarized as follows.

Overall, BET provides reasonable initial approximations of both net aerodynamic properties as well as aerodynamic modal forces.

Though BET lacks absolute quantitative accuracy, it is much more computationally efficient relative to conventional fluid modeling approaches. For the simulations carried out in this work, BET estimated aerodynamic modal forces five orders of magnitude faster than CFD. We found that for hovering flight kinematics, aerodynamic modal forces estimated via BET agreed fairly well both in magnitude and phase with those calculated via CFD. The largest error ( $\approx 50\%$ ) was in the magnitude of the primary frequency. We then addressed how well BET estimated aerodynamic modal forces for different flapping kinematics. We found that for small perturbations in rotation amplitude and phase, BET predicted modal forces fairly well. The agreement between CFD and BET began to break down for larger deviations from hovering flapping kinematics; however, these exaggerated cases are generally not characteristic of biological flight. We determined that inertial-elastic and aerodynamic modal forces are generally on the same order of magnitude and that inertial-elastic forces are larger for bending modes while aerodynamic forces are larger for torsional modes. However, additional efforts must be made to identify if bilateral fluid-structure coupling will significantly affect these findings.

To summarize, this novel FSI framework lays the foundation for optimal design of small flapping wing robotic vehicles and enables advanced studies in insect sensorimotor control. This work has demonstrated the feasibility of low-order flapping wing FSI models and has contributed to the understanding of the physics that govern insect wing deformation. Moving forward, we must consider other flight regimes such as forward flight and incorporate more realistic FEA models of insect wings.

## Acknowledgment

This material is based upon work supported by the National Science Foundation (NSF) (Grant No. CBET-1855383; Funder ID: 10.13039/501100008982). Any opinions, findings, and conclusions or recommendations expressed in this material are those of the author(s) and do not necessarily reflect the views of the NSF.

## **Nomenclature**

k = turbulent kinetic energy

r =spanwise position of the blade element

P =fluid pressure

W = out-of-plane elastic deformation

A = angle of attack  $\vec{V} = \text{blade element velocity}$ 

 $q_k = k$ th modal response

 $u_i = i$ th component direction of the fluid velocity

 $Q_k = k$ th aerodynamic modal force

c(r) = wing chord width

dm = differential mass element

dr = blade element differential length

 $\vec{a_k}$ ,  $\vec{b_k} = k$ th inertial force center vector

 $dS_w$  = blade element differential area

 $x_{LE}$ ,  $x_{TE}$  = wing leading/trailing edge

 $C_D$ ,  $C_L = \text{drag/lift coefficients}$ 

 $F_A$ ,  $F_N$  = aerodynamic axial/normal forces

 $F_L$ ,  $F_D$  = aerodynamic lift/drag forces

 $\alpha$  = roll rotation

 $\beta$  = pitch rotation

 $\gamma$  = yaw rotation

 $\mu = \text{dynamic viscosity}$ 

 $\mu_t = \text{eddy (turbulent) viscosity}$ 

 $\rho_f$  = fluid density

 $\tau$  = Reynolds stress tensor

 $\phi_{\underline{k}} = k$ th vibration mode

 $\vec{\Omega}$  = angular velocity vector

 $\omega_k = k$ th natural frequency

## Appendix: Approximate Analytic Solution

We rely primarily on numerical techniques to solve the linear time-varying equation of motion described by Eq. (18). However, it is prudent to develop an approximate analytic solution to verify the accuracy of our numerical results. We use the harmonic balance method to determine the periodic, steady-state solution of Eq. (18). Note that because of the assumed periodicity, this method cannot identify (1) parametric resonances associated with the periodically varying stiffness or (2) system instability, which may arise if the stiffness coefficient averaged over a wingbeat is negative. The approximate analytic solution is derived as follows. We represent Eq. (18) in the form

$$\ddot{q} + g(t)q = f(t) \tag{A1}$$

where q is the kth modal response (subscript dropped for clarity), g(t) is a general time-varying stiffness term, and f(t) is a general modal force. Each term can be represented via a complex Fourier series such that

$$q(t) = \sum_{n = -\infty}^{\infty} Q_n e^{jn\omega t}$$
 (A2)

$$f(t) = \sum_{k = -\infty}^{\infty} F_k e^{jk\omega t}$$
 (A3)

$$g(t) = \sum_{m=-\infty}^{\infty} G_m e^{2jm\omega t}$$
 (A4)

where  $Q_n$ ,  $F_k$ , and  $G_m$  are complex Fourier coefficients. We assume the primary component of g(t) varies at twice the flapping frequency  $\omega$ . Coefficients  $F_k$  and  $G_k$  are known because the flapping kinematics are prescribed, and therefore, we must solve only for  $Q_n$  to characterize the response. We substitute the above Fourier series into Eq. (A1) and equate similar terms. This forms the linear algebra problem

$$\mathbf{A}(G_m)\vec{O} = \vec{F} \tag{A5}$$

where  $A(G_m)$  is a square matrix containing known coefficients  $G_m$ . Then,  $\vec{Q} = [Q_{-n} \cdots Q_{-1}, Q_0, Q_1 \cdots Q_n]^T$  and  $\vec{F} = [F_{-k} \cdots F_{-1}, F_0, F_1 \cdots F_k]^T$ . Equation (A5) can be readily be solved to determine the unknown modal response coefficients  $Q_n$ . Specific to our problem, we assume a three-term Fourier expansion of the modal response, modal force, and stiffness. We consider the flapping kinematics shown in Table 3 and assume the flapping to occur in air. We solve Eq. (18) both numerically and via our approximate method. The comparison between solutions for the first and second modal responses is shown in Fig. 12. Overall, the agreement

Normalized First Modal Response vs. Wingbeat

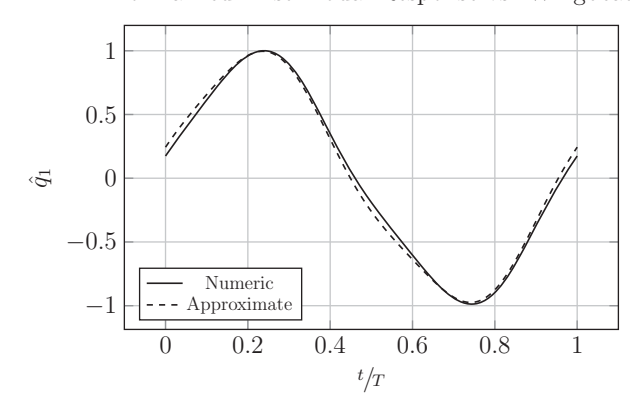


Fig. 12 Comparison between the approximate analytic solution and the numeric solution for the first modal response

**Transactions of the ASME** 

is quite good, both in terms of magnitude and phase. The modest difference can be reconciled by assuming a higher-order Fourier expansion; however, harmonics greater than  $5\omega$  are very small for all modal forces observed for hovering flight kinematics.

## References

- [1] Trimmer, W. S., 1989, "Microrobots and Micromechanical Systems," Sens. Actuators, 19(3), pp. 267–287.
- [2] Fuller, S. B., Karpelson, M., Censi, A., Ma, K. Y., and Wood, R. J., 2014, Controlling Free Flight of a Robotic Fly Using An Onboard Vision Sensor Inspired by Insect Ocelli," J. R. Soc. Interface, 11(97), p. 20140281.
- [3] Wood, R. J., 2008, "The First Takeoff of a Biologically Inspired At-Scale Robotic Insect," IEEE Trans. Robot., 24(2), pp. 341–347.
- [4] Combes, S. A., and Daniel, T. L., 2003, "Into Thin Air: Contributions of Aerodynamic and Inertial-Elastic Forces to Wing Bending in the Hawkmoth Manduca Sexta," J. Exp. Biol., 206(17), pp. 2999–3006
- [5] Young, J., Walker, S. M., Bomphrey, R. J., Taylor, G. K., and Thomas, A. L., 2009, "Details of Insect Wing Design and Deformation Enhance Aerodynamic Function and Flight Efficiency," Science, 325(5947), pp. 1549–1552.
  [6] Du, G., and Sun, M., 2010, "Effects of Wing Deformation on Aerodynamic
- Forces in Hovering Hoverflies," J. Exp. Biol., 213(13), pp. 2273-2283.
- [7] Jankauski, M., Guo, Z., and Shen, I., 2018, "The Effect of Structural Deformation on Flapping Wing Energetics," J. Sound. Vib., 429, pp. 176-192.
- [8] Dickerson, B. H., Aldworth, Z. N., and Daniel, T. L., 2014, "Control of Moth Flight Posture is Mediated By Wing Mechanosensory Feedback," J. Exp. Biol., 217(13), pp. 2301-2308.
- [9] Fu, J., Liu, X., Shyy, W., and Qiu, H., 2018, "Effects of Flexibility and Aspect Ratio on the Aerodynamic Performance of Flapping Wings," Bioinspir. Biomim., 13(3), p. 036001.
- [10] Dickinson, M. H., and Tu, M. S., 1997, "The Function of Dipteran Flight Muscle," Comp. Biochem. Physiol. A, 116(3), pp. 223-238.
- [11] Tuthill, J. C., and Wilson, R. I., 2016, "Mechanosensation and Adaptive Motor Control in Insects," Curr. Biol., 26(20), p. R1022.
- [12] Norris, A. G., 2013, "Experimental Characterization of the Structural Dynamics and Aero-Structural Sensitivity of a Hawkmoth Wing Toward the Development of Design Rules for Flapping-Wing Micro Air Vehicles," Air Force Institute of Technology, Technical Report.
- [13] Fairuz, Z., Abdullah, M., Yusoff, H., and Abdullah, M., 2013, "Fluid Structure Interaction of Unsteady Aerodynamics of Flapping Wing At Low Reynolds Number," Eng. Appl. Comput. Fluid Mech., 7(1), pp. 144–158.
  [14] Ishihara, D., Horie, T., and Denda, M., 2009, "A Two-Dimensional
- Computational Study on the Fluid-Structure Interaction Cause of Wing Pitch
- Changes in Dipteran Flapping Flight," J. Exp. Biol., 212(1), pp. 1–10.
  [15] Nakata, T., and Liu, H., 2012, "Aerodynamic Performance of a Hovering Hawkmoth With Flexible Wings: A Computational Approach," Proc. R. Soc. B, **279**(1729), pp. 722–731.
- [16] Pfeiffer, A. T., Lee, J.-S., Han, J.-H., and Baier, H., 2010, "Ornithopter Flight Simulation Based on Flexible Multi-Body Dynamics," J. Bionic Eng., 7(1), pp. 102-111.
- [17] Jankauski, M., and Shen, I., 2014, "Dynamic Modeling of an Insect Wing Subject to Three-Dimensional Rotation," Int. J. Micro Air Veh., 6(4), pp. 231-251
- [18] Sane, S. P., and Dickinson, M. H., 2002, "The Aerodynamic Effects of Wing Rotation and a Revised Quasi-Steady Model of Flapping Flight," J. Exp. Biol., **205**(8), pp. 1087–1096.
- [19] Dickinson, M. H., Lehmann, F.-O., and Sane, S. P., 1999, "Wing Rotation and the Aerodynamic Basis of Insect Flight," Science, 284(5422), pp. 1954-1960.
- [20] Truong, Q., Nguyen, Q., Truong, V., Park, H., Byun, D., and Goo, N., 2011, "A Modified Blade Element Theory for Estimation of Forces Generated By a
- Beetle-Mimicking Flapping Wing System," Bioinspir. Biomim., 6(3), p. 036008. [21] Berman, G. J., and Wang, Z. J., 2007, "Energy-Minimizing Kinematics in Hovering Insect Flight," J. Fluid Mech., 582, pp. 153-168.

- [22] Jankauski, M., Daniel, T., and Shen, I., 2017, "Asymmetries in Wing Inertial and Aerodynamic Torques Contribute to Steering in Flying Insects," Bioinspir. Biomim., 12(4), p. 046001.
- [23] Whitney, J. P., and Wood, R. J., 2010, "Aeromechanics of Passive Rotation in Flapping Flight," J. Fluid Mech., 660, pp. 197-220.
- [24] Wang, Q., Goosen, J., and van Keulen, F., 2017, "An Efficient Fluid-Structure Interaction Model for Optimizing Twistable Flapping Wings," J. Fluids Struct., **73**, pp. 82–99.
- [25] Stanford, B., Kurdi, M., Beran, P., and McClung, A., 2012, "Shape, Structure, and Kinematic Parameterization of a Power-Optimal Hovering Wing," J. Aircraft, 49(6), pp. 1687-1699.
- [26] Suzuki, T., and Mahfuz, H., 2018, "Analysis of Large-Scale Ocean Current Turbine Blades Using Fluid-Structure Interaction and Blade Element Momentum Theory," Ships Offshore Struct., 13(5), pp. 451-458.
- [27] Johnson, W., 2013, Rotorcraft Aeromechanics, Vol. 36, Cambridge University Press, Cambridge.
- Norlin, J., and Järpner, C., 2012, "Fluid Structure Interaction on Wind Turbine Blades," Ph.D. thesis, Master's thesis in Solid and Structural Mechanics and Fluid Dynamics, Chalmers University of Technology, Gothenburg, Sweden.
- Bottasso, C. L., Bortolotti, P., Croce, A., and Gualdoni, F., 2016, "Integrated Aero-Structural Optimization of Wind Turbines," Multibody Syst. Dyn., 38(4), pp. 317-344
- [30] Chin, D. D., and Lentink, D., 2016, "Flapping Wing Aerodynamics: From Insects to Vertebrates," J. Exp. Biol., 219(7), pp. 920-932
- Shyy, W., Aono, H., Chimakurthi, S. K., Trizila, P., Kang, C.-K., Cesnik, C. E., and Liu, H., 2010, "Recent Progress in Flapping Wing Aerodynamics and Aeroelasticity," Prog. Aerospace Sci., 46(7), pp. 284-327.
- [32] Sedov, L. I., Chu, C., Cohen, H., Seckler, B., and Gillis, J., 1965, "Two-Dimensional Problems in Hydrodynamics and Aerodynamics," Phys. Today, 18(12), pp. 62-63.
- [33] Zikanov, O., 2010, Essential Computational Fluid Dynamics, John Wiley & Sons, New York.
- Spalart, P., and Allmaras, S., 1992, "A One-Equation Turbulence Model for Aerodynamic Flows," 30th Aerospace Sciences Meeting and Exhibit, Reno, NV, Jan. 6-9, p. 439.
- [35] Wilcox, D., 2002, Turbulence Modeling for CFD, 2nd ed., DCW Industries, Anaheim, CA.
- [36] Hadzic, H., 2006, "Development and Application of Finite Volume Method for the Computation of Flows Around Moving Bodies on Unstructured, Overlapping Grids," Ph.D. thesis, Technische Universität Hamburg, Hamburg.
- [37] Combes, S., and Daniel, T., 2003, "Flexural Stiffness in Insect Wings. II. Spatial Distribution and Dynamic Wing Bending," J. Exp. Biol., 206(17), pp. 2989–2997.
- [38] Sims, T. W., Palazotto, A. N., and Norris, A., 2010, "A Structural Dynamic Analysis of a Manduca Sexta Forewing," Int. J. Micro Air Veh., 2(3), pp. 119-140.
- [39] Willmott, A. P., and Ellington, C. P., 1997, "The Mechanics of Flight in the Hawkmoth Manduca Sexta. I. Kinematics of Hovering and Forward Flight," J. Exp. Biol., 200(21), pp. 2705–2722.
- [40] Platzer, M., and Jones, K., 2006, "Steady and Unsteady Aerodynamics," Flow Phenomena in Nature, Vol. 4, WIT Transactions on State-of-the-Art in Science and Engineering, WIT Press, Southampton, UK, pp. 531-541.
- [41] Nakata, T., Liu, H., and Bomphrey, R. J., 2015, "A CFD-Informed Quasi-Steady Model of Flapping-Wing Aerodynamics," J. Fluid Mech., 783, pp. 323-343.
- [42] Pohly, J., Salmon, J., Bluman, J., Nedunchezian, K., and Kang, C.-K., 2018, "Quasi-Steady Versus Navier-Stokes Solutions of Flapping Wing Aerodynamics," Fluids, 3(4), p. 81.
- [43] Hedrick, T. L., and Daniel, T., 2006, "Flight Control in the Hawkmoth Manduca Sexta: The Inverse Problem of Hovering," J. Exp. Biol., 209(16), pp. 3114–3130.
- [44] Alexandra Yarger, J. F., 2016, "Dipteran Halteres: Perspectives on Function and Integration for a Unique Sensory Organ," Integr. Comp. Biol., 56(5), pp. 865-876.
- [45] Nakata, T., and Liu, H., 2011, "Aerodynamic Performance of a Hovering Hawkmoth With Flexible Wings: A Computational Approach," Proc. R. Soc. B: Biol. Sci., 279(1729), pp. 722-731.